AAS 22-741

LEVERAGING INTERMEDIATE DYNAMICAL MODELS FOR TRANSITIONING FROM THE CIRCULAR RESTRICTED THREE-BODY PROBLEM TO AN EPHEMERIS MODEL

Beom Park* **and Kathleen C. Howell†**

While the Earth-Moon Circular Restricted Three-body Problem (CR3BP) provides useful dynamical structures that are successfully leveraged for actual missions, transitioning the CR3BP solutions into a higher-fidelity ephemeris model remains nontrivial. The transitioning procedure may benefit by more consistently incorporating information from an intermediate model. This work examines the Elliptic Restricted Three-Body Problem (ER3BP) and Bi-Circular Restricted Four-Body Problem (BCR4BP) as the intermediate models that potentially bridge the gap between the CR3BP and a higher-fidelity ephemeris model. The value of these models within the context of a transition is investigated, and some sample transitions are demonstrated.

INTRODUCTION

The dynamical structures that exist in the Earth-Moon Circular Restricted Three-Body Problem (CR3BP) are integral to multiple types of missions in cislunar space. Libration points and the associated periodic or quasi-periodic orbits may serve as science orbits to meet various objectives. For example, the Acceleration, Reconnection, Turbulence and Electrodynamics of the Moon's Interation with the Sun (ARTEMIS) spacecraft successfully leveraged Lissajous orbits around both L_1 and L_2 for multiple heliophysics and planetary objectives in 2010.[1] In the near future, JAXA's EQUilibriUm Lunar-Earth point 6U Spacecraft (EQUULEUS) plans to utilize an L_2 quasi-halo orbit to demonstrate the trajectory control capabilities for a CubeSat.[2] The Gateway mission, as proposed by NASA, is also expected to deliver a hub-like facility into an L_2 9:2 Near Rectilinear Halo Orbit (NRHO), leveraging the stability and eclipse properties of the orbit.[3]

While the CR3BP offers diverse structures suited for a variety of missions and enables mission design in a simplified dynamical environment, a higher-fidelity model that is critical for flight inevitably introduces additional forces. In the cislunar space environment, assuming a point-mass model for the celestial bodies, some of the most impactful forces originate from the non-uniform pulsation of the Earth-Moon system ("pulsation") and any additional gravitational bodies, mainly the Sun. Depending on the region, these forces may be non-negligible and can impact the solution significantly. Thus, transitioning the CR3BP dynamical structures into their counterparts or analogs within a higher-fidelity model can be a nontrivial process. Numerical procedures that leverage differential correctors are typically employed, often paired with optimizers to enforce desired characteristics[2] or to minimize the deviation from the original solution designed within the CR3BP.[4,5]

Given an orbit or trajectory that is constructed in the CR3BP, transitioning such a solution to a higher-fidelity dynamical model without leveraging any intermediate models, is termed here as a "direct" approach. As the additional forces are unmodeled in the CR3BP, the direct approach relies on the specifics of the numerical schemes to produce successful results. Multiple patchpoints, rather than a single patchpoint, are

*Ph.D. Student, School of Aeronautics and Astronautics, Purdue University, West Lafayette, IN 47907; park1103@purdue.edu
†Hsu Lo Distinguished Professor of Aeronautics and Astronautics, School of Aeronautics and Astronautics, Purdue University, West Lafayette, IN 47907; howell@purdue.edu

frequently utilized, where the original CR3BP solution is discretized and transformed to an initial guess within a higher-fidelity model. The transformation procedure typically involves a rotation and dimensionalization process, where the instantaneous distance between the gravitational bodies is retrieved from the ephemerides and aids in an appropriate scaling process.[2,6] The results of the transition also depend on other components of the numerical schemes including the number of patchpoints, propagation direction, and the baseline epoch for the transition.[7,8] The direct approach offers a simple yet versatile transition method that produces desired results for many regions throughout cislunar space. However, due to the innate limitations of the CR3BP to incorporate some of the additional forces into the solution, the direct approach may require more "trial-and-error" steps with different numerical formulations. This endeavor, for example, includes searching for a favorable baseline epoch when the desired characteristics are better preserved; as the CR3BP is a time-independent model, it provides only limited information regarding the epoch. Furthermore, previous authors[7,9] note that some periodic orbits in the Earth-Moon L_2 halo family, e.g., those close to the 3:1 synodic resonance, do not maintain their geometry within a higher-fidelity model, which serves as a sample case where the direct transition is particularly challenging.

One alternative to the direct approach is a strategy to explicitly incorporate intermediate models that potentially bridge the gap between the CR3BP and a higher-fidelity ephemeris model. For example, Lantoine and Russell[10] introduce a continuation method, where intermediate models are constructed by introducing the interpolated positions of the gravitational bodies originating from the CR3BP and evolving into the ephemeris model. A number of periodically perturbed Hamiltonian systems are also employed as intermediate models that introduce an additional force in an ideal form, generally governed by one frequency. These models include, but are not limited to, the Elliptic Restricted Three-Body Problem (ER3BP), the Bi-Circular Restricted Four-Body Problem (BCR4BP), and the Quasi Bi-Circular four-body Problem (QBCP). For example, Peng and Bai[11] leverage halo orbits within the ER3BP for an ephemeris transition with application to constellation design. Boudad, Howell and Davis[9] demonstrate that dynamical structures from the BCR4BP offer an enhanced guess for the 3:1 synodic resonance halo region, where the direct transition is challenging. Dei Tos and Topputo[12] discuss the advantages of utilizing the ER3BP and BCR4BP as intermediate steps for smoother transition. Jorba-Cuscó, Farrés, and Jorba[13] examine the potential benefits of incorporating the BCR4BP and QBCP for examining the dynamics near the libration points within a higher-fidelity model. Finally, intermediate models with multiple added frequencies are constructed for a more accurate approximation of the actual dynamics. Gómez, Masdemont, and Mondelo[14] identify five basic frequencies in the Earth-Moon system to construct an intermediate model and produce dynamical substitutes for collinear libration points. Similarly, Hou and Liu[15,16] leverage intermediate models with four frequencies to analyze the motion of spacecraft near both collinear and triangular libration points in an ephemeris model.

While multiple formulations for the intermediate models are possible, the current investigation focuses on the ER3BP and BCR4BP, hereby denoted "intermediate models" for simplicity. In addition to the CR3BP dynamics, these two models include the conic pulsation of the primaries, and the gravity of an ideal Sun within a circular orbit around the Earth-Moon barycenter, respectively. These models are selected as extensions to the CR3BP that incorporate additional forces due to pulsation and the solar gravity in ideal forms. These are periodically-perturbed Hamiltonian systems, where the periodic orbits in the CR3BP generally evolve into periodic orbits or quasi-periodic orbits.[17] Thus, it is possible to systematically assess and characterize the impact of the ideal additional perturbing forces.[18,19] Moreover, the unique structures within these models may bridge the gap that exists between the CR3BP and a higher-fidelity ephemeris model and serve as effective evolving initial guesses for transition, particularly when maintaining the characteristics of the lower-fidelity solution is critical. While other variations of the restricted problem potentially offer similar benefits, the ER3BP and BCR4BP are selected since they are relatively simple to construct and appear more frequently in previous research investigations.

The goal of the current effort is a strategy and an assessment of the ER3BP and BCR4BP as intermediate models for the transitioning process from the CR3BP to a higher-fidelity ephemeris model. In the literature,[9,11] a bottom-up approach is typically adopted, i.e., sample transition cases that successfully leverage these intermediate models are reported. This work employs a top-down approach; the ephemeris dynamics is analyzed first and facilitates the subsequent assessment of the ER3BP and BCR4BP. A careful evaluation

of these models is warranted, as incorporating the intermediate models inevitably adds complexity as compared to a direct transition from the CR3BP. Since the intermediate models introduce the additional forces into the CR3BP only in ideal forms, they are not guaranteed to be "more accurate" for a given epoch or system configuration. Moreover, the ER3BP still does not model any solar gravity, and similarly, the BCR4BP does not incorporate pulsation. Hence, the capabilities of the intermediate models to evolve the solution to the full ephemeris representation are expected to depend on a number of factors and consideration of these issues warrants more analysis: (1) identification of the impact of the additional forces on an arc within a higher-fidelity model, (2) evaluation of the the ER3BP and the BCR4BP models to represent the respective additional forces in a more global sense within cislunar space, and (3) demonstration of the procedure to incorporate these models for a successful ephemeris transition process.

The analysis is organized as follows. The dynamical models are initially defined, where the Equations Of Motion (EOMs) are cast within a common coordinate frame to facilitate analysis. Then, the EOMs are rearranged to yield more intuition concerning the effects of the additional forces within an ephemeris model. The capabilities and limitations of the ER3BP and BCR4BP in describing the respective additional forces are noted. Finally, the applicability of the ER3BP and the BCR4BP within the Earth-Moon system is demonstrated by introducing a sample transition process from a lower- to higher-fidelity model.

DYNAMICAL MODELS

In the current investigation, the focus involves four dynamical models: CR3BP, ER3BP, BCR4BP, and the Higher-Fidelity Ephemeris Model (HFEM). The differential equations governing the behavior in the HFEM are typically represented in an inertial frame, e.g., J2000 frame, whereas the restricted multi-body problems are typically cast within a rotating frame where the primaries, Earth and the Moon, are located at fixed positions. To cope with this discrepancy, Gómez, Masdemont, and Mondelo[14] introduce a pulsating-rotating frame where the HFEM is now represented in a similar form as compared to the CR3BP, but under realistic perturbations from the additional forces, a formulation that is well-suited for the current work. The definition of the pulsating-rotating frame is reviewed, followed by a common form of the EOMs for the various models that are under investigation within this frame. The assumptions and the analytical expressions for the coefficients in the EOMs for each model are provided. Finally, the isochronous correspondence between the models, necessary to accomodate the different independent variables in the models, is also detailed.

Inertial Frame and Pulsating-Rotating Frame

The relationship between the inertial frame and the pulsating-rotating frame is first constructed. Without losing generality, the spacecraft (s/c) is under the gravitational influence of Earth and the Moon, i.e., the primaries, and the additional bodies that are incorporated in the model. By assumption, a point-mass model is utilized for the gravitational bodies. Subscripts E, M, and j denote Earth, the Moon and the additional bodies, respectively, where j is an element of the set of additional bodies, $\mathcal{A}$. For example, if the Sun is included as the only additional body, $\mathcal{A} = \{\text{Sun}\}$. An inertial frame is illustrated in Figure 1(a), where the origin O is located at an inertially fixed point, which may be defined differently depending on the models. Unit vectors $\hat{X} - \hat{Y} - \hat{Z}$ define the mutually perpendicular directions, where carets identify unit vectors. The dimensional position vector for the s/c with respect to O is denoted $\vec{R}$ (all vectors are denoted with an overarrow.) Within this frame, the dimensional position vector from Earth to the Moon is expressed as $\vec{R}_{EM}$. The barycenter, i.e., the center of mass between Earth and the Moon, is denoted B, where $\vec{B}$ corresponds to the position vector for B with respect to O. The position vector from B to the s/c is denoted $\vec{R}_{Bc}$, where subscripts B and c correspond to the barycenter and the s/c, respectively. Then, consider a second frame as illustrated in Figure 1(b), denoted the pulsating-rotating frame, where the origin is now located at B. The unit vectors, $\hat{x} - \hat{y} - \hat{z}$, are constructed as,

$$\hat{x} = \frac{\vec{R}_{EM}}{l}, \qquad \hat{y} = \hat{z} \times \hat{x}, \qquad \hat{z} = \frac{\vec{h}}{h}, \tag{1}$$

where l is the magnitude of $\vec{R}_{EM}$, or the dimensional distance between Earth and the Moon. The angular momentum vector reflecting the primary motion, $\vec{h}$, is computed as $\vec{h} = \vec{R}_{EM} \times \vec{V}_{EM}$, where $\times$ denotes

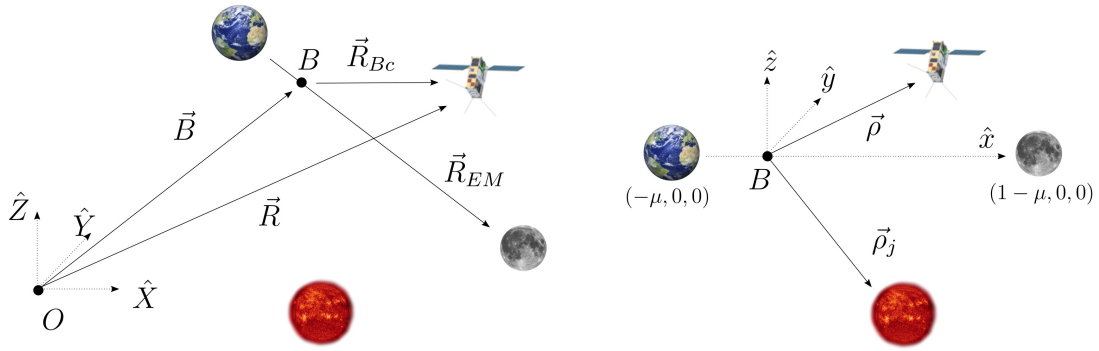

(a) Inertial frame

(b) Pulsating-rotating frame

Figure 1: Frames under investigation

the cross product and $\vec{V}_{EM}$ is the dimensional velocity expressed in terms of the inertial frame, i.e., $\vec{V}_{EM} = \vec{R}'_{EM} = d\vec{R}_{EM}/dT$, where the prime denotes the derivative with respect to the dimensional time, T. The magnitude of $\vec{h}$ is denoted h. The value for l, or the dimensional distance between Earth and the Moon, potentially pulsates as the Earth-Moon motion evolves within the inertial frame. However, the Earth-Moon distance within the pulsating-rotating frame is always nondimensionalized to be unit magnitude. Consistent with the rotation of the frame, Earth and the Moon lie on the $\hat{x}$-axis at fixed positions, $(-\mu, 0, 0)$ and $(1-\mu, 0, 0)$, respectively. The mass ratio μ is computed as $\mu = \tilde{\mu}_M/(\tilde{\mu}_E + \tilde{\mu}_M)$, where $\tilde{\mu}$ denotes the dimensional gravitational parameter of the respective bodies. Within the pulsating-rotating frame, the nondimensional s/c position vector is represented as $\vec{\rho} = x\hat{x} + y\hat{y} + z\hat{z}$. Then, without losing generality, the relationship between the position vectors within two frames is retrieved as,

$$\vec{R} = \vec{B} + l\boldsymbol{C}\vec{\rho}, \tag{2}$$

where the appropriate direction cosine matrix $\boldsymbol{C}$ is evaluated as, $\boldsymbol{C} = \begin{bmatrix}\hat{x} & \hat{y} & \hat{z}\end{bmatrix}$. (All matrices are bold.) Note that no assumptions are introduced to the models to derive this relationship; it is valid for all models under investigation. Equation (2) consists of three components: translation of the origin, $\vec{B}$, dimensionalization via the pulsating distance, l, and rotation with the direction cosine matrix, $\boldsymbol{C}$. These components are generally functions of T and are evaluated at each instant to construct the pulsating-frame given the states of the gravitational bodies. The time history of the states are evaluated differently depending on the models. The nondimensional velocity of the s/c, as viewed and expressed in terms of the appropriate frame, is represented by $\dot{\vec{\rho}}$, where the dot represents the differentiation of $\vec{\rho}$ with respect to the nondimensional time, t. Similarly, the nondimensional acceleration of the s/c with respect to the pulsating frame is represented by $\ddot{\vec{\rho}}$. The notations for two independent variables, i.e., T and t, are summarized in Table 1 for clarification.

Table 1: Notations for two independent variables

	Dimensional time	Nondimensional time
Symbol	T	t
Derivative symbol	$\frac{d(\cdot)}{dT} = (\cdot)'$	$\frac{d(\cdot)}{dt} = \dot{(\cdot)}$
Associated frame	Inertial frame (Figure 1(a))	Pulsating-rotating frame (Figure 1(b))

Equations of Motion

The EOMs for motion of the s/c within the context of the pulsating-rotating frame, i.e., expressions for $\ddot{\vec{\rho}}$, are produced for any models under investigation. To derive the EOMs in a common framework for all the

models, differentiate Eq. (2) twice with respect to the dimensional time, T. The first and second derivatives result in the following,

$$\vec{R}' = \vec{B}' + l'\boldsymbol{C}\vec{\rho} + l\boldsymbol{C}'\vec{\rho} + l\boldsymbol{C}\vec{\rho}' \tag{3}$$

$$\vec{R}'' = \vec{B}' + (l''\boldsymbol{C} + 2l'\boldsymbol{C}' + l\boldsymbol{C}'')\vec{\rho} + (2l'\boldsymbol{C} + 2l\boldsymbol{C}')\vec{\rho}' + l\boldsymbol{C}\vec{\rho}'', \tag{4}$$

respectively. While this process is consistent with the Newtonian derivation, the Lagrangian derivation is also possible.[14] Note that $\vec{B}, l, \boldsymbol{C}$ are functions of T, in general, and it is natural to include derivatives with respect to dimensional time T. However, as expressions for $\ddot{\vec{\rho}}$ are desired, the transformation between derivatives of $\vec{\rho}$ with respect to dimensional and nondimensional times, i.e., T and t, is detailed. The first and second derivatives are related by,

$$\frac{d\vec{\rho}}{dT} = \vec{\rho}' = \frac{d\vec{\rho}}{dt}\frac{dt}{dT} = \dot{\vec{\rho}} \cdot t' \tag{5}$$

$$\frac{d^2\vec{\rho}}{dT^2} = \vec{\rho}'' = \ddot{\vec{\rho}} \cdot t'^2 + \dot{\vec{\rho}} \cdot t'', \tag{6}$$

respectively. Then, Eq. (4) is solved for $\ddot{\vec{\rho}}$ to render,

$$\ddot{\vec{\rho}} = -\frac{1}{t'}[(\frac{2l'}{l} + \frac{t''}{t'})\boldsymbol{I} + 2\boldsymbol{C}^\intercal\boldsymbol{C}']\dot{\vec{\rho}} - \frac{1}{t'^2}[\frac{l''}{l}\boldsymbol{I} + \frac{2l'}{l}\boldsymbol{C}^\intercal\boldsymbol{C}' + \boldsymbol{C}^\intercal\boldsymbol{C}'']\vec{\rho} + \frac{1}{lt'^2}\boldsymbol{C}^\intercal(\vec{R}'' - \vec{B}''), \tag{7}$$

where superscript $\intercal$ denotes the transpose of a matrix, and $\boldsymbol{I}$ corresponds to a three-by-three identiy matrix. Gomez, Masdemont, and Mondelo[14] also introduce an alternative representation of Eq. (7) with a set of coefficients, i.e., the following form,

$$\ddot{\vec{\rho}} = \begin{bmatrix} b_1 \\ b_2 \\ b_3 \end{bmatrix} + \begin{bmatrix} b_4 & b_5 & 0 \\ -b_5 & b_4 & b_6 \\ 0 & -b_6 & b_4 \end{bmatrix}\dot{\vec{\rho}} + \begin{bmatrix} b_7 & b_9 & b_8 \\ -b_9 & b_{10} & b_{11} \\ b_8 & -b_{11} & b_{12} \end{bmatrix}\vec{\rho} + b_{13}\nabla\Omega, \tag{8}$$

where and b_{1-13} correspond to a set of coefficients that are evaluated differently across models but with this same formulation of the EOMs. Note that $\nabla\Omega$ is the gradient of a potential function Ω that is evaluated from,

$$\Omega = \Omega(\mu, \vec{\rho}, \mathcal{A}, \mu_j, \vec{\rho}_j) = \frac{1-\mu}{\rho_{Ec}} + \frac{\mu}{\rho_{Mc}} + \sum_{j\in\mathcal{A}}\frac{\mu_j}{\rho_{jc}}, \tag{9}$$

where the nondimensional gravitational parameter for $j \in \mathcal{A}$, μ_j, is computed as $\mu_j = \tilde{\mu}_j/(\tilde{\mu}_E + \tilde{\mu}_M)$. The different analytical expressions for b_{1-13} for each model are provided in Table 2. These expressions are assessed within the context of the assumptions for the respective model as follows.

HFEM The HFEM is introduced first, as the expressions for the coefficients in the HFEM apply for other models as well, where the terms simplify depending on the assumptions introduced in the lower-fidelity models. For the HFEM, the set $\mathcal{A}$ is comprised of the Sun and the rest of the planets in the solar system. It is assumed to be a coherent model, where the six-dimensional states and the epoch for the gravitational bodies under their mutual gravitational influence are well-approximated by the ephemerides from the SPICE libraries.[20] Then, the solar system barycenter is the origin, O, for the inertial frame in the HFEM. The analytical expressions for the coefficients for the HFEM are summarized in the second column of Table 2. Note that the coefficients are evaluated with a number of quantities retrieved from the ephemerides. For example, b_{1-3} are related to the acceleration of B within the inertial frame, i.e., $\vec{B}'' = -\sum_{j\in\mathcal{A}}\left(\frac{\tilde{\mu}_j(1-\mu)}{R_{jE}^3}\vec{R}_{jE} + \frac{\tilde{\mu}_j\mu}{R_{jM}^3}\vec{R}_{jM}\right)$, where the barycenter is influenced by the bodies within $\mathcal{A}$. Additionally, in Table 2, $\vec{A}_{EM}$ and $\vec{J}_{EM}$ correspond to the acceleration and jerk of the Moon with respect to Earth, respectively, or, $\vec{A}_{EM} = \vec{R}''_{EM}$ and $\vec{J}_{EM} = \vec{R}'''_{EM}$. Note that these quantities are not directly retrieved from the ephemerides, as the SPICE

Table 2: Coefficients in the EOMs for the models under investigation

	HFEM	CR3BP	ER3BP	BCR4BP
b_1	$-\frac{\vec{B}''\cdot\hat{x}}{(t')^2 l}$	0	0	$-\frac{\mu_S}{\rho_{S*}^2}\cos\theta_S$
b_2	$-\frac{\vec{B}''\cdot\hat{y}}{(t')^2 l}$	0	0	$-\frac{\mu_S}{\rho_{S*}^2}\sin\theta_S$
b_3	$-\frac{\vec{B}''\cdot\hat{z}}{(t')^2 l}$	0	0	0
b_4	$-\frac{l'}{2t'l}$	0	$-\frac{e\sin f}{2\sqrt{1+e\cos f}}$	0
b_5	$\frac{2h}{t'l^2}$	2	$2\sqrt{1+e\cos f}$	2
b_6	$\frac{2l}{t'h}\vec{A}_{EM}\cdot\hat{z}$	0	0	0
b_7	$-\frac{l''}{(t')^2 l}+\frac{h^2}{(t')^2 l^4}$	1	1	1
b_8	$-\frac{1}{(t')^2 l}\vec{A}_{EM}\cdot\hat{z}$	0	0	0
b_9	$\frac{h'}{(t')^2 l^2}$	0	0	0
b_{10}	$-\frac{l''}{(t')^2 l}+\frac{h^2}{(t')^2 l^4}+\frac{l^2}{(t')^2 h^2}(\vec{A}_{EM}\cdot\hat{z})^2$	1	1	1
b_{11}	$\frac{3hl'-2lh'}{(t')^2 h^2}\vec{A}_{EM}\cdot\hat{z}+\frac{l}{(t')^2 h}\vec{J}_{EM}\cdot\hat{z}$	0	0	0
b_{12}	$-\frac{l''}{(t')^2 l}+\frac{l^2}{(t')^2 h^2}(\vec{A}_{EM}\cdot\hat{z})^2$	0	$-e\cos f$	0
b_{13}	$\frac{\tilde{\mu}_E+\tilde{\mu}_M}{l^3(t')^2}=1$	$\frac{\tilde{\mu}_E+\tilde{\mu}_M}{l_*^3(t_*')^2}=1$	$\frac{\tilde{\mu}_E+\tilde{\mu}_M}{l^3(t')^2}=1$	$\frac{\tilde{\mu}_E+\tilde{\mu}_M}{l_*^3(t_*')^2}=1$

data only includes up to the first derivative of the position, i.e., the velocity, $\vec{V}_{EM}$. Thus, these higher-order derivatives are manually constructed assuming the point-mass model for the gravitational bodies. The remaining quantities in the coefficient expressions depend on derivatives of l, h, and t, also constructed from the ephemerides. For detailed derivations for these quantities, refer to Dei Tos.[21] Since the HFEM does not assume a simplified motion for the gravitational bodies, the nondimensional analytical expressions for many coefficients are not necessarily reduced to constants, e.g., one. Rather, they are constructed by the instantaneously retrieved information from the ephemerides depending on T.

CR3BP For the CR3BP, only the Earth and the Moon are included as the gravitational bodies in the model. The Moon is orbiting around Earth in a circular orbit with a radius of l_*, denoted as the characteristic length. The characteristic time, $1/t_*'$, is constructed such that $l_*^3(t_*')^2/(\tilde{\mu}_E+\tilde{\mu}_M)=1$. Employing Eq. (2) by nondimensionalizing the distance with l_* and time with $1/t_*'$, the following EOMs are produced with respect to the pulsating-rotating frame,[22]

$$\ddot{\vec{\rho}}=-2\hat{z}\times\dot{\vec{\rho}}+\nabla\Omega_C, \tag{10}$$

where Ω_C is the pseudo-potential function for the CR3BP, computed as $\Omega_C=(x^2+y^2)/2+\Omega$, where Ω is evaluated with $\mathcal{A}=\varnothing$, or an empty set, as additional gravitational bodies are not included within the CR3BP. The CR3BP depends on only one parameter, μ, and is a time-independent system. In the current work, the μ value is selected to be consistent with the SPICE data, i.e., $\mu\approx 0.01215$. Note that $\vec{B}$ is a zero vector since the barycenter is an inertially fixed point for the CR3BP; it results in $b_{1-3}=0$, as these terms involve the acceleration of B within the inertial frame, i.e., $\vec{B}''$. Many other coefficients are simplified since $l'=h'=0$, as l and h do not vary for a circular orbit of the Moon around Earth, as assumed in the CR3BP. Therefore, a majority of the coefficients simplify to zeros, except the following notable terms: $b_5=2$ (Coriolis), $b_7=b_{10}=1$ (centrifugal), and $b_{13}=1$ (gravity from the primaries).

ER3BP The ER3BP currently assumes a conic orbit for the Moon around Earth, where no additional gravitational bodies are present, or, $\mathcal{A}=\varnothing$. The semi-major axis for the conic is assumed to be l_*, the characteristic length for the CR3BP, with an eccentricity value of e. Introducing a new independent variable,

then, the following EOMs are developed with respect to the true anomaly, f,[22] i.e.,

$$\frac{d^2\vec{\rho}}{df^2} = -2\hat{z} \times \frac{d\vec{\rho}}{df} + \nabla\Omega_E, \tag{11}$$

where Ω_E is the pseudo-potential function for the ER3BP, evaluated as $\Omega_E = \frac{1}{1+e\cos f}\Omega_C - \frac{e\cos f}{1+e\cos f} \cdot \frac{z^2}{2}$. Switching the independent variable from f to the nondimensional time t, the EOMs for the ER3BP are derived as,

$$\ddot{\vec{\rho}} = -\frac{e\sin f}{2\sqrt{(1+e\cos f)}}\dot{\vec{\rho}} - 2\hat{z} \times \dot{\vec{\rho}}\sqrt{1+e\cos f} - e\cos f z\hat{z} + \nabla\Omega_C, \tag{12}$$

where the added complexities are apparent in comparison to the CR3BP, as l is not constant as modeled within the ER3BP. As a result, some of the coefficients from Table 2 are evaluated with terms containing e and f, but, note that the expressions are much simpler in contrast to the HFEM. The relative simplicity is due to the fact that a conic orbit leads to $h' = 0$. Similar to the CR3BP, as additional bodies are not present, B is considered an inertially fixed point and b_{1-3} are still zeros. Yet, due to the appearance of f in the EOMs, the ER3BP is a time-dependent system where $\dot{f} = \sqrt{1+e\cos f}$, with a nondimensional period of 2π, also denoted the sidereal period. The ER3BP is fully defined by two pararameters, μ and e, as well as the initial value for f.

BCR4BP The BCR4BP incorporates the solar gravity into the CR3BP dynamics. In addition to the assumptions in the CR3BP, the BCR4BP models the Sun and B both as following circular paths around their mutual barycenter, B_S, where all the gravitational bodies are moving in the same plane. By assumption, the Sun does not exert a gravitational force on Earth and the Moon directly, but it influences B; thus, the BCR4BP is not a coherent model. The constant, nondimensional distance between the Sun and B is denoted ρ_{S*}. Then, the nondimensional position vector of the Sun within the pulsating-rotating frame is expressed as, $\vec{\rho}_S = \rho_{S*}\cos\theta_S\hat{x} + \rho_{S*}\sin\theta_S\hat{y}$, where θ_S denotes the angle between $\hat{x}$-axis and $\vec{\rho}_S$, also labeled the Sun angle. The Sun angle changes at a constant rate in the BCR4BP, or, $\dot{\theta}_S = 1 - n_S$, where $n_S = \sqrt{\frac{\tilde{\mu}_S+\tilde{\mu}_E+\tilde{\mu}_M}{(\tilde{\mu}_E+\tilde{\mu}_M)\rho_{S*}^3}}$. The EOMs representing the BCR4BP within the pulsating-rotating frame yield,[23]

$$\ddot{\vec{\rho}} = -2\hat{z} \times \dot{\vec{\rho}} + \nabla\Omega_B, \tag{13}$$

where Ω_B is the pseudo-potential function for the BCR4BP, evaluated as $\Omega_B = (x^2+y^2)/2 + \Omega - \Omega_{S,B}$. The potential function Ω is formulated with $\mathcal{A} = \{\text{Sun}\}$. Note that the last term, $\Omega_{S,B} = \mu_S/\rho_{S*}^2(x\cos\theta_S + y\sin\theta)$, originates from the gravitational acceleration of B due to the Sun, or,

$$\nabla\Omega_{S,B} = \frac{1}{l_*^2 t_*'}\boldsymbol{C}\vec{B}'' = -\frac{\tilde{\mu}_S}{l_*^2 t_*'}\frac{\boldsymbol{C}\vec{R}_{SB}}{R_{SB}^3} = \frac{\mu_S}{\rho_{S*}^3}\vec{\rho}_S. \tag{14}$$

Thus, the coefficients b_{1-3} for the BCR4BP are non-zero and depend on the location of the Sun within the pulsating-rotating frame. The rest of the coefficients for the BCR4BP are the same as in the CR3BP, as l and h in the BCR4BP are also constant. These constants occur by adding the Sun to the CR3BP in a manner that is not coherent, i.e., where the Moon remains in a circular orbit around Earth despite the presence of the Sun. Yet, the BCR4BP is a time-dependent system where the nondimensional period is $2\pi/(1-n_S)$, also denoted the synodic period. The BCR4BP is fully defined by three pararameters, μ, ρ_{S*}, and n_S, as well as the initial value for θ_S.

Isochronous Correspondence

While the EOMs from Eq. (8) provide a methodology to assess the dynamical models in a consistent formulation, the evaluation of the coefficients in Table 2 requires a definition for the relationship between the independent variables in the different models. For example, while the CR3BP EOMs in Eq. (10) evolve with the nondimensional time, t, the bodies within the HFEM depend on the dimensional time, T, as retrieving the SPICE data requires an epoch expressed in terms of T. Thus, writing the EOMs for the HFEM with respect

to t requires a definition for $t' = dt/dT$, a quantity that appears frequently in the expressions for b_{1-13}. It is emphasized that t' may be defined by any arbitrary function, as the CR3BP and HFEM are constructed independently; the expression for t' does not change the dynamical evolution in the models but deliver a suitable isochronous correspondence between the various models.

While there exists no precise definition for t', one formulation may be preferred over another for some numerical properties. One possible option for t' is an assumption to render a uniform flow of time, i.e.,

$$\textbf{Uniform flow of time} \quad t' = t'_* = \sqrt{\frac{\tilde{\mu}_E + \tilde{\mu}_M}{l_*^3}}, \tag{15}$$

where l_* is the constant, characteristic length from the CR3BP. One advantage of this formulation is the simplicity in computing t'' that appears in expressions for the coefficients that are related to $\dot{\vec{\rho}}$, i.e., $b_{7,10,12}$. Thus, the constant flow of time is typically adopted as in previous investigations[12,14,15] leveraging the EOMs within the pulsating-rotating frame. However, one noticeable drawback of this formulation is that, as the distance l pulsates, the quantity $l^3(t'_*)^2/(\tilde{\mu}_E + \tilde{\mu}_M)$ does not equal to one. Here, Gómez et al.[24] note that a coherence problem then occurs, as in the CR3BP, the core property of the nondimensionalization process is that $l_*^3(t'_*)^2/(\tilde{\mu}_E+\tilde{\mu}_M)$. As a consequence, when utilizing $t' = t'_*$ under a realistic pulsation of the primaries, the coefficient for the gravity from the primaries, b_{13}, is not consistently scaled to one but depends on the distance between the primaries.

In response to this correspondence problem, in the current work, a non-uniform flow of time is adopted instead. The relationship between t and T is defined as follows,

$$\textbf{Non-uniform flow of time} \quad t' = \sqrt{\frac{\tilde{\mu}_E + \tilde{\mu}_M}{l^3}}, \tag{16}$$

where t' is now a function of the pulsating distance, l, and automatically satisfies $l^3(t')^2/(\tilde{\mu}_E+\tilde{\mu}_M) = 1$. As a result, b_{13} is consistently evaluated as unity for all models under investigation. Utilizing this non-uniform flow of time also aids in the proper scaling for the transformation of the states between the inertial and pulsating-rotating frames. The following expression summarizes the transformation,

$$\begin{bmatrix} \vec{R} - \vec{B} \\ \vec{R}' - \vec{B}' \end{bmatrix} = \begin{bmatrix} l\boldsymbol{C} & \mathbf{0}_{3\times 3} \\ l'\boldsymbol{C} + l\boldsymbol{C}' & l\boldsymbol{C} \cdot t' \end{bmatrix} \begin{bmatrix} \vec{\rho} \\ \dot{\vec{\rho}} \end{bmatrix}, \tag{17}$$

where the rows correspond to Eq. (2) and Eq. (3), respectively. For given initial conditions in the CR3BP, $(\vec{\rho}_0, \dot{\vec{\rho}}_0)$, the initial guess within the HFEM is often delivered from the above equation.[2,6] It is noted that the dimensional inertial velocity expression, $\vec{R}' - \vec{B}'$, includes a term that scales $\dot{\vec{\rho}}$ by t'. Indeed, the initial guess for the velocity in the HFEM is inseparable from the relationship between the independent time variables, i.e., t'. Note that $(\vec{\rho}_0, \dot{\vec{\rho}}_0)$ evolves under the CR3BP dynamics and, intuitively, leveraging Eq. (16) aids in generating an initial guess in the HFEM that maintains the characteristics in the original CR3BP solution, as noted by many authors.[2,5,6,25] For the current investigation, it is desired to identify additional forces in the HFEM with respect to the CR3BP by writing the EOMs in the common formulation. Thus, a choice of t' that results in relatively small deviations of the coefficients between the HFEM and CR3BP facilitates the analysis and Eq. (16) is, thus, adopted. It automatically satisfies $l^3(t')^2/(\tilde{\mu}_E + \tilde{\mu}_M) = 1$; therefore, the coefficient for the gravity of the primaries, i.e., b_{13}, is consistently evaluated as unity, and velocity is also consistently scaled such that the difference in the coefficients is likely to be reduced. One small complexity in this formulation is the non-zero value of the t'' term. It is computed as $t'' = -\sqrt{(\tilde{\mu}_E + \tilde{\mu}_M)/l^5}\, l' = -3t'l'/2l$, and is straightforward to evaluate.

For completeness, the isochronous correspondence for the independent variables in the remaining two models, i.e., the ER3BP and the BCR4BP, is also important. For the ER3BP, the following relationship between f and t is constructed,

$$\dot{f} = \frac{f'}{t'} = \frac{h_E}{l_E^2}\sqrt{\frac{l_E^3}{\tilde{\mu}_E + \tilde{\mu}_M}} = \sqrt{1 + e\cos f}, \tag{18}$$

where h_E and l_E are the angular momentum and the Earth-Moon distance for the assumed conic motion of the Moon around Earth. The conic equation, i.e., $l_E = h_E^2/((\tilde{\mu}_E + \tilde{\mu}_M) \cdot (1 + e\cos f))$, is leveraged for the derivation. For the BCR4BP, it is straightforward to assume that the independent variable for the BCR4BP is the same as that of the CR3BP.

EVALUATION OF MODELS

The EOMs from Eq. (8) supply a common formulation of the dynamical models, where the coefficients b_{1-13} are evaluated differently for each model. As apparent from the expressions in Table 2, the HFEM coefficients consist of quantities that depend on time. The time history for the coefficients in the HFEM appear in Figure 2 over one year originating on 09/23/2023. Two coefficients are not included in the figure; b_{10} typically differs from b_7 by a very small amount that is not apparent visually in the scale of Figure 2(c), and b_{13} is computed as a constant number, i.e., one. As the coefficients for the HFEM display complex behavior, it is non-trivial to deduce simple patterns that aid in understanding the HFEM as a perturbed model of the CR3BP. In response to this problem, previous investigations focus on identifying the core frequencies in the coefficients via Fourier analysis.[12,14] Instead, the current work takes an analytical approach to further reduce the complexity of the expressions in Table 2 and to produce more intuitive patterns that facilitate the assessment of the value of incorporating the ER3BP and BCR4BP.

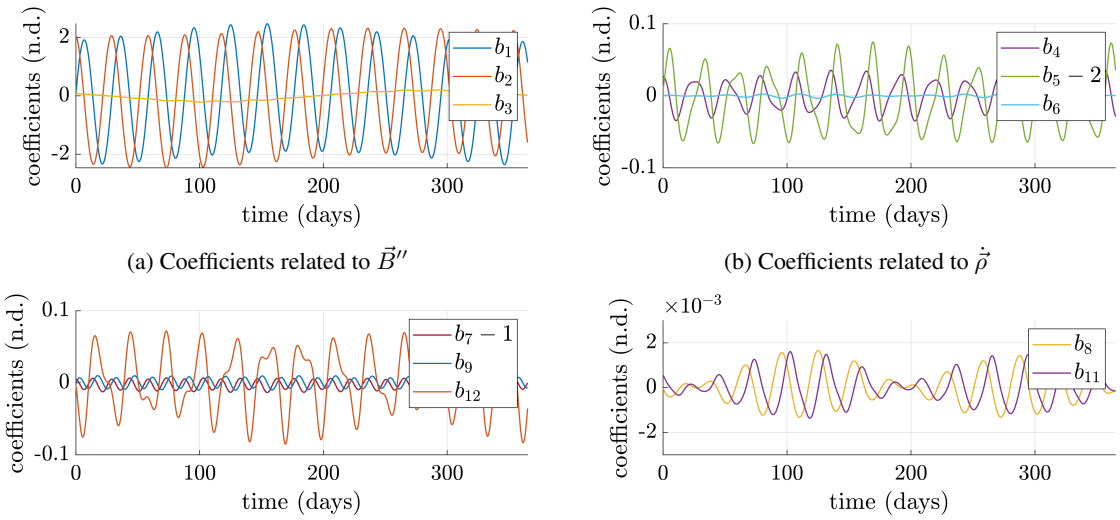

(a) Coefficients related to $\vec{B}''$

(b) Coefficients related to $\dot{\vec{\rho}}$

(c) Coefficients related to $\vec{\rho}$

(d) Coefficients related to $\vec{\rho}$ with smaller magnitudes

Figure 2: Time history for the coefficients in the HFEM beginning 09/23/2023 and ranging over one year

Rearranging the HFEM EOMs

The EOMs for the HFEM are rearranged such that cancellations occur among the complex coefficients, that also highlight the impact of the additional forces. The accelerations in the HFEM are categorized relevant to the three sources: (1) CR3BP, (2) pulsation, and (3) additional bodies, i.e.,

$$\ddot{\vec{\rho}}_H = \ddot{\vec{\rho}}_C + \ddot{\vec{\rho}}_{P,H} + \ddot{\vec{\rho}}_{\mathcal{A},H} \tag{19}$$

where the subscripts H, C, P, and $\mathcal{A}$ denote the HFEM, CR3BP, pulsation and additional bodies, respectively. Note that Eq. (19) is consistent with the isochronous correspondence defined by Eq. (16). This categorization of the terms is somewhat arbitrary, as the "true" pulsation is indeed inseparable from the gravitational influence due to the additional bodies. As the ER3BP incorporates a conic pulsation with $\mathcal{A} = \varnothing$, the additional terms in the ER3BP, as compared to the CR3BP, are initially identified as the acceleration originating from

pulsation. Observing the coefficients in the CR3BP and ER3BP, the pulsation acceleration is defined as,

$$\ddot{\vec{\rho}}_P := \ddot{\vec{\rho}}_E - \ddot{\vec{\rho}}_C = \begin{bmatrix} b_4 & b_5 - 2 & 0 \\ -b_5 + 2 & b_4 & 0 \\ 0 & 0 & b_4 \end{bmatrix} \dot{\vec{\rho}} + \begin{bmatrix} 0 & 0 & 0 \\ 0 & 0 & 0 \\ 0 & 0 & b_{12a} \end{bmatrix} \vec{\rho}, \tag{20}$$

where the subscript E denotes the ER3BP. These additional terms consist of $b_{4,5,12a}$ that are evaluated differently for the ER3BP and HFEM to retrieve $\ddot{\vec{\rho}}_{P,E}$ and $\ddot{\vec{\rho}}_{P,H}$, respectively. The coefficient b_{12a} is the first term in b_{12}, evaluated as $b_{12a} = -l''/(t'^2 l)$. These coefficients are primarily dependent on l, l' and l'', i.e., the quantities that are related to pulsation. As the BCR4BP does not incorporate pulsation into the model, this acceleration is evaluated as zero in the BCR4BP. The remaining the perturbing accelerations are then grouped and represented as originating from the inclusion of additional bodies, or,

$$\ddot{\vec{\rho}}_{\mathcal{A}} := \ddot{\vec{\rho}}_H - \ddot{\vec{\rho}}_C - \ddot{\vec{\rho}}_P = \begin{bmatrix} b_1 \\ b_2 \\ b_3 \end{bmatrix} + \begin{bmatrix} 0 & 0 & 0 \\ 0 & 0 & b_6 \\ 0 & -b_6 & 0 \end{bmatrix} \dot{\vec{\rho}} + \begin{bmatrix} b_7 - 1 & b_9 & b_8 \\ -b_9 & b_{10} - 1 & b_{11} \\ b_8 & -b_{11} & b_{12} - b_{12a} \end{bmatrix} \vec{\rho} + \nabla \sum_{j \in \mathcal{A}} \frac{\mu_j}{\rho_{jc}}, \tag{21}$$

where some of the terms are now approximated in the BCR4BP. In contrast, the ER3BP includes a zero acceleration for $\ddot{\vec{\rho}}_{\mathcal{A}}$ as additional bodies are not present in the model. Although grouping the "rest" of the terms is arbitrary to some degree, manipulation of Eq. (21) results in much simplified expressions that are dominated by the quantities associated with the additional bodies. Following the derivations in Appendix A, the equation is rewritten as,

$$\ddot{\vec{\rho}}_{\mathcal{A},H} = \ddot{\vec{\rho}}_{\mathcal{A},G} + \begin{bmatrix} 0 & 0 & 0 \\ 0 & 0 & b_6 \\ 0 & -b_6 & 0 \end{bmatrix} \dot{\vec{\rho}} + \begin{bmatrix} 0 & 0 & 0 \\ 0 & b_{12} - b_{12a} & b_{11} \\ 0 & -b_{11} & b_{12} - b_{12a} \end{bmatrix} \vec{\rho}, \tag{22}$$

where $\ddot{\vec{\rho}}_{\mathcal{A},G}$ denotes the "pseudo-gravity" term, evaluated as,

$$\ddot{\vec{\rho}}_{\mathcal{A},G} = -\sum_{j \in \mathcal{A}} \mu_j \left(\frac{\vec{\rho}_{jc}}{\rho_{jc}^3} + \frac{\vec{\rho}_{Mc} \cdot \hat{x}}{\rho_{jE}^3} \vec{\rho}_{jE} - \frac{\vec{\rho}_{Ec} \cdot \hat{x}}{\rho_{jM}^3} \vec{\rho}_{jM} - \frac{\vec{\rho}_{Mc} \cdot \hat{y}}{\rho_{jE}^3} (\vec{\rho}_{jE} \times \hat{z}) + \frac{\vec{\rho}_{Ec} \cdot \hat{y}}{\rho_{jM}^3} (\vec{\rho}_{jM} \times \hat{z}) - (\frac{z z_j}{\rho_{jE}^3} - \frac{z z_j}{\rho_{jM}^3}) \hat{x} \right). \tag{23}$$

The significance of this expression is that the terms only depend on $\vec{\rho}_j$ and $\vec{\rho}$, or, the position vectors of the additional bodies and the s/c in the pulsating-rotating frame, as the primaries are fixed within this frame. The terms also include the inverse cubes of the distance between the bodies; hence, they are labeled as the pseudo-gravity term. Many of the original expressions for the coefficients in Eq. (21) cancel to result in this simplified formulation; as the HFEM is assumed to be a coherent model, the coefficients all essentially originate from the mutual gravitational influences of the bodies. While the cancellation happens between b_{1-3}, b_{7-10} and $\nabla \sum_{j \in \mathcal{A}} (\mu_j / \rho_{jc})$, the remaining terms do not necessarily transform into simple expressions. These terms correspond to $b_{6,11}$, and $b_{12} - b_{12a}$ in Eq. (22). While these coefficients involve some non-trivial terms that are challenging to evaluate, e.g., $\vec{J}_{EM} \cdot \hat{z}$, they are typically associated with relatively small magnitudes as compared to the other coefficients. Also, the pseudo-gravity acceleration involves pairs of similar expressions that reflect the subtraction of terms dependent on $\vec{\rho}_{jM}$ from terms involving $\vec{\rho}_{jE}$. Noting these characteristics, Eq. (22) is further simplified with the following assumptions: (1) the additional bodies exert negligible forces except the Sun, (2) the Sun is far from B, i.e., $\rho_S >> 1$, and (3) the out-of-plane component of the Sun's position within the pulsating-rotating frame is negligible in comparison to the in-plane components, or, $|z_S| << \rho_S$. Then, as deduced from the the derivations in Appendix B, Eq. (22) is simplified as,

$$\ddot{\vec{\rho}}_{\mathcal{A},H} \approx \ddot{\vec{\rho}}_{\mathcal{A},L} = \frac{3\mu_S}{\rho_S^5} \left(2 x_S y_S y \hat{x} + (y_S^2 - x_S^2) y \hat{y} \right), \tag{24}$$

where the subscript L denotes linearization. If $\rho_S^2 \approx x_S^2 + y_S^2$, or the out-of-plane component of the Sun's position is negligible, $\ddot{\rho}_{\mathcal{A},L} = 3\mu_S / \rho_S^3 |y|$, i.e., the magnitude of the solar perturbation varies linearly with the y-excursion of the s/c within the pulsating-rotating frame. Denoting the Sun's position vector as $\vec{\rho}_S \approx$

$\rho_S \cos\theta_S \hat{x} + \rho_S \sin\theta_S \hat{y}$, where θ_S is the Sun angle that is defined consistent with the BCR4BP, Eq. (24) is equivalently expressed as,

$$\ddot{\vec{\rho}}_{\mathcal{A},L} = \frac{3\mu_S}{\rho_S^3} y(\sin 2\theta_S \hat{x} - \cos 2\theta_S \hat{y}), \tag{25}$$

where it is notable that $2\theta_S$ appears in the trigonometry functions. To validate this result, consider three contour plots in Figure 3, corresponding to $\ddot{\vec{\rho}}_{\mathcal{A},L}$, $\ddot{\vec{\rho}}_{\mathcal{A},H}$, and difference between two accelerations. These acceleration expressions are investigated at multiple points constructed within the $\hat{x} - \hat{y}$ plane, assuming that z and $\dot{\vec{\rho}}$ are both zero in magnitude and the zero vector, respectively. In the plots, the white circles denote the primaries, i.e., Earth and the Moon and the red x's correspond to the five Lagrange points. The color of the plots denotes the acceleration magnitude computed at each location, and the cyan arrows note the direction of the acceleration vector. The contour plots correspond to an epoch on 09/23/2023, when $\theta_S \approx -105°$, as illustrated by an orange arrow aligned with the direction of the Sun within the frame. From the plots, it is notable that the linearized acceleration, $\ddot{\vec{\rho}}_{\mathcal{A},L}$, is closely aligned with the original acceleration direction, $\ddot{\vec{\rho}}_{\mathcal{A},H}$, where the differences are orders of magnitude smaller as compared to the scale of $\ddot{\vec{\rho}}_{\mathcal{A},H}$. Approximately, the magnitude varies linearly with the y-excursion of the s/c, resulting in negligible perturbing accelerations near the $\hat{x}$-axis but more significant in the $L_{4,5}$ regions, where the y-excursion is approximately 0.87 in the nondimensional unit (n.d.). In these regions, the acceleration magnitude exceeds 0.01 n.d., comparable to an acceleration level that a low-thrust engine is able to provide, e.g., Intuitive Machine's Khon-1 s/c,[26] which also approximately produces an acceleration level of 0.01 n.d., implying a non-negligible acceleration magnitude. The direction of the acceleration is computed as,

$$\arctan_2(-\text{sgn}(y)\cos 2\theta_S, \text{sgn}(y)\sin 2\theta_S) = -90° + 2\theta_S \ (y > 0) \text{ or } 90° + 2\theta_S \ (y < 0), \tag{26}$$

where $\arctan_2$ is a four quadrant arctangent and sgn is a sign function. From the plots, it is apparent that the cyan arrows generally align with the above angles. While the form in Eq. (25) is counter-intuitive, it indeed represents the gravitational influence of the Sun on the s/c in the pulsating-rotating frame under a coherent model.

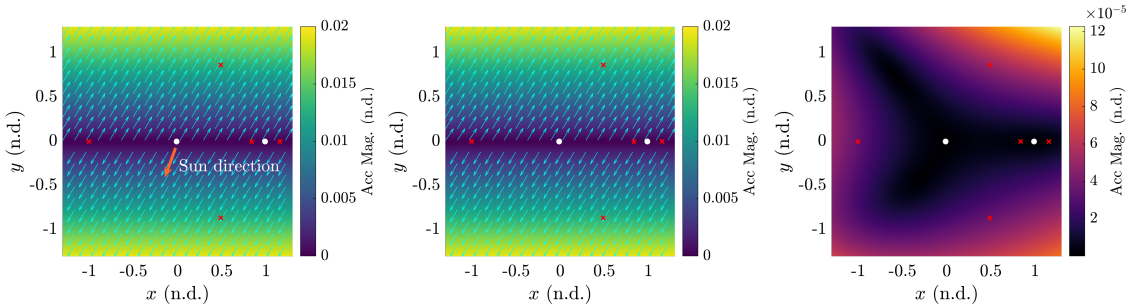

Figure 3: Contour plots for $\ddot{\vec{\rho}}_{\mathcal{A},L}$ (left), $\ddot{\vec{\rho}}_{\mathcal{A},H}$ (center), and $\ddot{\vec{\rho}}_{\mathcal{A},H} - \ddot{\vec{\rho}}_{\mathcal{A},L}$ (right), epoch: 09/23/2023

Assessment of the ER3BP

The capabilities and limitations of the ER3BP to serve as an intermediate frame are assessed in terms of $\ddot{\vec{\rho}}_P$. Note that as additional bodies are not included in the ER3BP, i.e., $\mathcal{A} = \varnothing$, the ER3BP only provides a zero estimate for $\ddot{\vec{\rho}}_{\mathcal{A}}$. As $\ddot{\vec{\rho}}_P$ is principally dependent on the velocity of the s/c, i.e., $\dot{\vec{\rho}}$, an arc that is propagated within the ER3BP is expected to deviate more from the arc within the HFEM when (1) the velocity magnitude is relatively small and (2) y-excursion is relatively large, such that $\ddot{\vec{\rho}}_{\mathcal{A}}$ is non-negligible. However, as the relative magnitudes of $\ddot{\vec{\rho}}_P$ and $\ddot{\vec{\rho}}_{\mathcal{A}}$ are path-dependent, it is first assumed that $|\ddot{\vec{\rho}}_{\mathcal{A}}| \approx 0$ to facilitate analysis. Then, the ER3BP is assessed in terms of $b_{4,5,12a}$, as these coefficients constitute the acceleration from pulsation, i.e., $\ddot{\vec{\rho}}_P$. These terms are comprised of several time-varying quantities, including l, h, and l'. For illustration, the time history for these quantities in the HFEM is plotted in Figure 4 over two years,

given an epoch 09/23/2023. Clearly, these quantities are not periodic and are known to incorporate multiple frequencies for a reasonable approximation,[27] where one of the frequencies roughly corresponds to the sidereal period. Thus, the capabilities and limitations of the ER3BP depend on the approach to approximate these non-periodic quantities with only one frequency governed by the sidereal period, i.e., 2π in t. The value of the ER3BP as an intermediate model in cislunar space also depends on two user-selected variables for the model: the eccentricity, e, and the initial true anomaly, f_0. Under the definition of the isochronous correspondence from Eq. (18), the semi-major axis for the elliptical orbit of the Moon around Earth, l_E, does not appear explicitly in the coefficients for the ER3BP.

For illustration, consider a sample value of $e = 0.055$ for the initial epoch $09/23/2023$, where the initial true anomaly is based on the osculating orbital elements of the lunar orbit around Earth at the epoch. In Figure 5, the grey lines correspond to the difference in $b_{4,5,12a}$ between the HFEM and CR3BP models over two years. The red lines note the difference in the coefficients for the HFEM and ER3BP. In this sample case, the ER3BP provides better estimates for the coefficients for approximately one year, after which its ability to reflect the evolution of the HFEM deteriorates. This tendency holds for other epochs in general; over time, the conic motion of the Moon becomes out-of-sync from the realistic lunar motion for the HFEM and the ER3BP does not suitably reflect the evolution of the osculating quantities, in comparison to the CR3BP, at least, in terms of the coefficients. While "re-initializing" the ER3BP with new values of e and f_0 may provide an approach to properly update the ER3BP in response to the realistic pulsation, it remains out-of-scope for this work. Rather, the values for e and f_0 are assumed to be fixed over a certain duration, i.e., one year. Figure 6 illustrates the average difference between the coefficients under different values for e and f_0 over one year, starting from 09/23/2023. The x-axis corresponds to the difference in the initial true anomaly, denoted as Δf, measured from the true anomaly provided by the osculating orbital elements at the initial epoch. The y-axis denotes the eccentricity value and the color illustrates the average difference between the coefficient values for the HFEM and ER3BP, where darker regions correspond to better matched combinations of f_0 and e over the time span. The contours appear as concentric circles surrounding the combination that results in the minimum average difference, where the specific patterns only slightly vary for each coefficient. As e approaches zero, the ER3BP reduces to the CR3BP; at this epoch, the ER3BP indeed offers an improved estimate for the coefficients over the given time interval on average, as compared to the CR3BP. Extending this analysis to multiple initial epochs, the minimum combinations are recorded for each initial epoch and plotted in Figure 7, where the initial epochs are constructed between 09/23/2023 and 09/23/2024 with a step size of $1/4$ days. Figure 7(a) demonstrates that an eccentricity value between 0.05 and 0.056 is typically desired, and the desirable values evolve with only small deviations across epoch for all three coefficients. On the contrary, Figure 7(b) illustrates that the initial true anomaly value sometimes requires a significant adjustment for proper initialization (note that plots for three coefficients are indistinguishable in this scale); for some epochs, utilizing the osculating true anomaly results in the ER3BP that offers less value when compared to the CR3BP. The troughs of the plot, i.e., epochs when more adjustments are required for f_0, correspond to the perigee of the Moon's motion around Earth, and vice versa. Approximately, when the Moon is at the apogee, utilizing $f_0 = 180^\circ$ typically provides a reasonable estimate. Indeed, additional analysis is warranted to examine different initialization schemes for f_0; such is not the focus of the current work. However, assuming that the true anomaly is initialized properly, it is clear that the ER3BP improves the estimate for the perturbing acceleration from pulsation as compared to the CR3BP on average over this finite span of time, i.e., one year; the patterns of concentric circles persist for all epochs with the center located at eccentricity values between 0.05 and 0.056. Of course, while better approximation for the coefficients indicates that the ER3BP potentially bridges the gap between the CR3BP and HFEM, its impact on the actual transition process remains unclear. As the transition process leverages a differential corrector that displays chaotic behavior in general, the solutions from the ER3BP are not always guaranteed to provide more accurate initial guesses for the HFEM. Still, the ER3BP is expected to provide some useful insights on the evolution of the CR3BP solutions under the additional accelerations originating from pulsation.

Assessment of the BCR4BP

Similar to the ER3BP evaluation, the capabilities and limitations of the BCR4BP as an intermediate model are assessed in terms of the acceleration from the additional bodies. i.e., $\ddot{\vec{\rho}}_{\mathcal{A}}$. For the BCR4BP, the accelera-

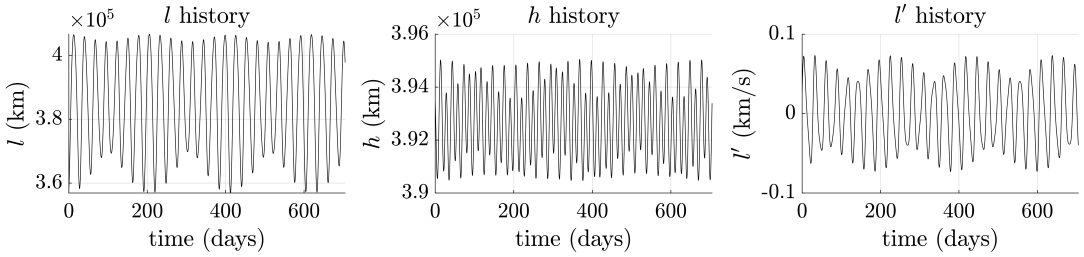

Figure 4: History of l, h, l' for the HFEM, starting epoch: 09/23/2023

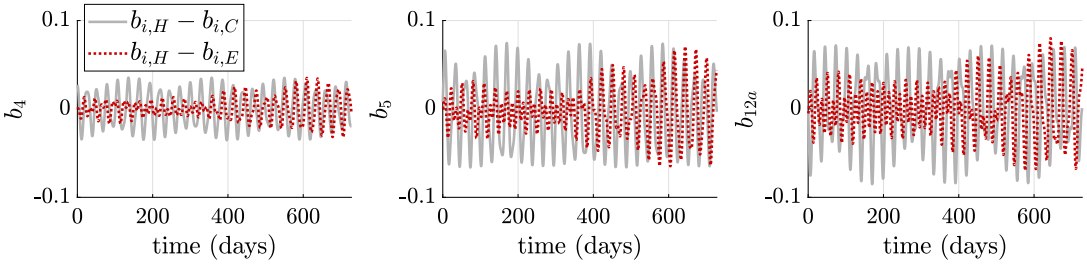

Figure 5: Comparison of coefficients for 2 years, starting epoch: 09/23/2023

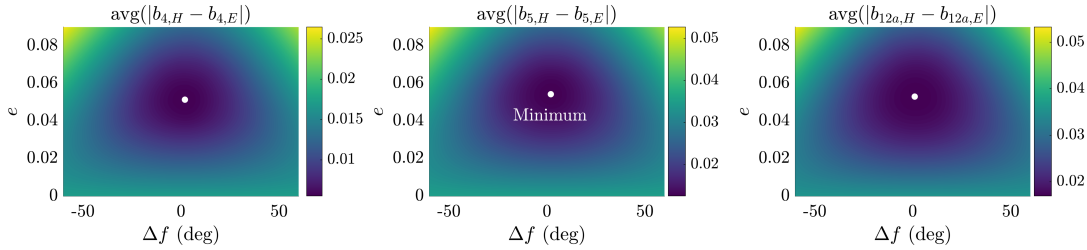

Figure 6: Average (avg) for the difference in the coefficients values, epoch: 09/23/2023

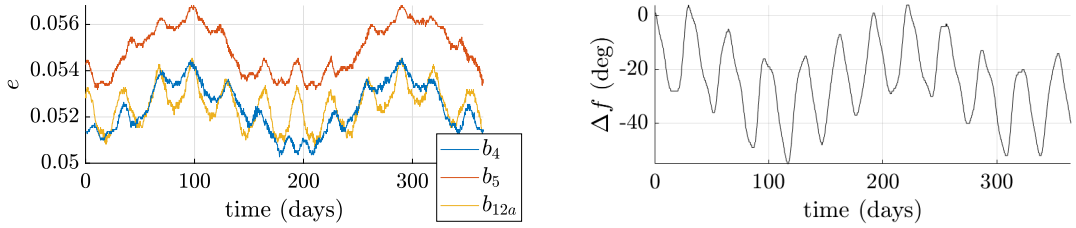

(a) e (b) Δf

Figure 7: Values of e and Δf associated with the minimum difference of coefficients, starting epoch: 09/23/2023

tion is evaluated as,

$$\ddot{\vec{\rho}}_{\mathcal{A},4} = -\frac{\mu_S}{\rho_{S*}^3}\vec{\rho}_S - \frac{\mu_S}{\rho_{Sc}^3}\vec{\rho}_{Sc}, \tag{27}$$

where subscript 4 denotes the BCR4BP. The first term corresponds to the gravitational influence of the Sun on B, and the second term denotes the direct influence of the Sun on the s/c. In general, the BCR4BP does not accurately estimate the $\ddot{\vec{\rho}}_{\mathcal{A}}$ from the HFEM. For illustration, consider the contour plots in Figure 8, where $\ddot{\vec{\rho}}_{\mathcal{A}}$ is compared between the BCR4BP and HFEM; the instantaneous values $\theta_S \approx -105°$, $\rho_{S*} \approx 388$

n.d., $n_S \approx 0.074$ n.d. are employed to construct the BCR4BP. Regardless of these values, however, the contour plots for the BCR4BP and HFEM display noticeably different patterns. While the magnitude of $\ddot{\vec{\rho}}_{\mathcal{A},4}$ gradually increases in the radial direction from B, the magnitude of $\ddot{\vec{\rho}}_{\mathcal{A},H}$ is mainly dependent on the y-excursion. As a result, the difference between the accelerations from the two models results in non-negligible magnitudes across cislunar space. This tendency holds for all epochs, where the concentric circle patterns in the third plot only slightly rotate and pulsate depending on the selected epoch. This difference originates from the fact that the BCR4BP is not constructed in a coherent manner. For the HFEM, expressions for b_{1-3} are partly cancelled by b_{7-12}, resulting in the linear relationship described in Eq. (24). However, while the BCR4BP incorporates some solar perturbations in the form of coefficients b_{1-3}, it only provides constant values for b_{7-12} that do not cancel b_{1-3}. Thus, the challenge in the use of the BCR4BP as an intermediate model is apparent. It does not completely bridge the gap between the coefficients for the CR3BP and HFEM, and it does not always characterize the dynamics adequately within the pulsating-rotating frame across the entire cislunar space. While Jorba-Cuscó, Farrés, and Jorba[13] discuss the challenges of the BCR4BP for analyzing the motion in the vicinity of the collinear equilibrium points, here, the challenge also persists for the triangular equilibrium points. It is noted, however, that the BCR4BP still offers an extremely useful model for analyzing the motion of a s/c in the exterior region of the Earth-Moon system, where the geometries of the BCR4BP solutions within the Sun-B rotating frame serve as viable initial guesses for the HFEM transition. However, in the interior region, the solutions from the BCR4BP do not necessarily enhance the initial guesses as compared to the CR3BP solutions. When the BCR4BP supplies a unique solution that deviates from the original CR3BP solution within the pulsating-rotating frame, the geometry change is driven by $\ddot{\vec{\rho}}_{\mathcal{A},4}$ that, generally, is an inadequate approximation for $\ddot{\vec{\rho}}_{\mathcal{A},H}$.

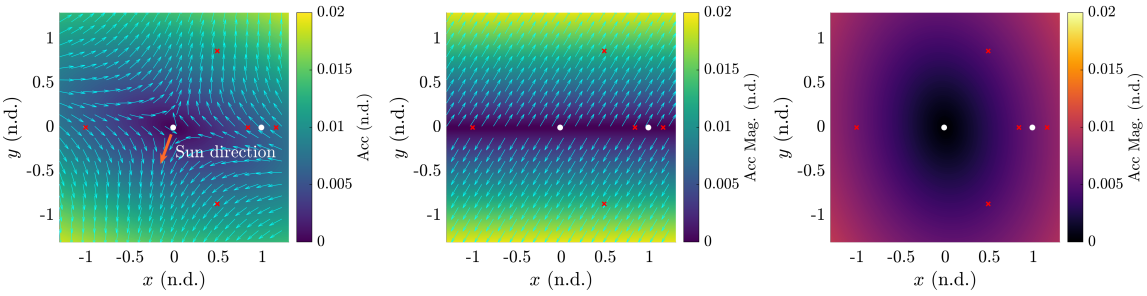

Figure 8: Contour plots for $\ddot{\vec{\rho}}_{\mathcal{A},4}$ (left), $\ddot{\vec{\rho}}_{\mathcal{A},H}$ (center), and $\ddot{\vec{\rho}}_{\mathcal{A},H} - \ddot{\vec{\rho}}_{\mathcal{A},4}$ (right), epoch: 09/23/2023

TRANSITION TO A HIGHER-FIDELITY EPHEMERIS MODEL FOR A SAMPLE ORBIT

While the investigation of the coefficients for the EOMs offers useful intuition regarding the additional perturbations in the HFEM and the capabilities of the ER3BP and BCR4BP, it requires further validation. As noted before, the small relative values of the coefficients do not necessarily guarantee that the solutions from the intermediate models are better preserved in the HFEM. Also, the comparison of the coefficients requires an isochronous correspondence definition, potentially a limiting assumption in any actual transition from a lower-fidelity model to the HFEM. Typically, the independent variables, or times, are incorporated as parts of the initial guess for the transition process; subsequently, the time variables are also under adjustments. Thus, for further validation, a sample transition problem is introduced, where a ballistic CR3BP orbit is directly transitioned into the HFEM. For demonstration, the L_2 southern halo orbit family serves as the basis for the sample scenario. The first plot in Figure 9 illustrates some CR3BP periodic orbits belonging to the family, colored differently according to the period of the orbits. When transitioned to the HFEM, the periodicity of the original solution is no longer guaranteed. To preserve the geometry of the original periodic orbits, one common practice is to stack multiple revolutions of the orbits and enforce continuity along the trajectory, utilizing a multiple shooting algorithm.[7] This strategy locates possible structures within the HFEM in the vicinity of the stack of orbits; a minimum-norm solution is typically employed to locate suitable arcs that are geometrically very similar without explicitly incorporating an optimizer. Utilizing such techniques, sample

solutions in the HFEM are produced by directly transitioning the selected L_2 halo orbits from the CR3BP, as illustrated in the second plot of Figure 9. For fast computation, only the Sun is incorporated as the additional body in the HFEM. Noted by previous authors,[7,9] some members of the family in a particular region evolve into solutions that deviate significantly from the original CR3BP solutions when transitioned to the HFEM in comparison with the majority of the members of the family. While this challenging region is not well bounded, orbits with periods ranging between 9 and 10 days tend to converge to solutions with behavior in the HFEM that appears more random.

For an orbit in the Earth-Moon L_2 halo family in the CR3BP for which direct transitions are challenging, the ER3BP potentially mitigates the issue, as deduced from the analysis of the coefficients. The maximum y-excursions of the halo orbits are relatively small and, thus, $\ddot{\vec{\rho}}_{\mathcal{A}}$ is typically associated with relatively small magnitudes as compared to $\ddot{\vec{\rho}}_P$ along the path of a halo orbit in the HFEM, implying that the evolution of the solutions in this region is likely to be driven by pulsation; the ER3BP potentially provides a model that bridges the gap between the CR3BP and HFEM in this region. As an enhanced initial guess, an analog of the CR3BP periodic orbit within the ER3BP is examined. The CR3BP periodic orbits evolve into periodic orbits in the ER3BP only when the period of the orbit is in resonance with the sidereal period and such an orbit is first identified. The third plot of Figure 9 illustrates the CR3BP orbit associated with a period that is $1/3$ of the sidereal period, in green. In the same plot, the red orbit corresponds to the ER3BP counterpart, where it requires exactly one sidereal period to complete one orbit that consists of three distinct lobes or revolutions around the Moon. An eccentricity value of $e = 0.055$ is leveraged to produce the periodic orbit. For more information about constructing the ER3BP periodic orbits, refer to Ferrari and Lavagna.[19] For this specific orbit, the timing of the apolune in the middle lobe coincides with an epoch when the Moon is at the apogee within its conic motion, i.e., $f = 180^\circ$, as required by the mirror configuration of the system.[19]

Then, a direct transition is initially attempted from the CR3BP to HFEM, solely utilizing the original CR3BP solution as the initial guess. For a consistent analysis, the following parameters are commonly employed in the multiple shooting algorithm: 12 revolutions of the orbit are stacked starting from the apolune, each revolution consists of five segments that are equally divided in t, and the reference (baseline) epoch is fixed to correspond to the apolune of the innermost (7th) revolution. Sample results are provided in Figure 10, corresponding to three different reference epochs. The original periodic structure from the CR3BP evolves into somewhat random solutions in the HFEM depending on the epoch, that is not explained solely by the CR3BP. It is notable that a distinct three-lobe geometry also appears for some reference epochs.

For comparison with a direct transition, the ER3BP is leveraged as an intermediate model, where the ER3BP counterpart or analog periodic orbit is now incorporated as an initial guess for the transition. The same formulations are utilized for the orbit stacking process, except that four revolutions of the ER3BP orbit are stacked as each revolution of the orbit is comprised of three lobes. For the baseline epoch, the construction of ER3BP periodic orbit requires that the apolune on the middle lobe occur at an epoch when $f = 180^\circ$. As noted previously, an epoch when the Earth-Moon distance is at a local maximum, i.e., apogee, suffices as a reasonable guess for the reference epoch. Sample results are depicted in Figure 11, where three selected epochs are apart by approximately one sidereal period, i.e., 27.5 days. In comparison with the direct transition approach, leveraging the ER3BP as an intermediate model provides several benefits for this sample orbit. First, visually, the solutions transitioned from the ER3BP are more tightly converged, a desirable characteristic when repeated geometry for the solution within the pulsating-rotating frame is warranted. Also, as indicated by the change in the geometry from the respective periodic orbits, the transition from the ER3BP typically requires fewer iterations during the corrections process; on average, the ER3BP transition requires six iterations in comparison to 12 iterations for the CR3BP transition. For the sample cases, the error from violating the continuity constraint monotonically decreases for the ER3BP, whereas the CR3BP requires a few initial iterations before the corrector locates a basin of attraction. This "smooth" transition is desired as it generally prevents the differential corrector from randomly converging into a HFEM solution that is not necessarily an analog of the original solution from the lower-fidelity models. Next, the ER3BP offers some systematic understanding of the evolution of the CR3BP structures under pulsation. Note that the ER3BP periodic orbit is associated with a three-lobe geometry that accurately approximates the evolution of the original CR3BP periodic orbit into the HFEM. Thus, even when the ER3BP solutions

are not directly leveraged as an enhanced initial guess for the HFEM transition, they do offer insight into the potential geometry changes under pulsation. The CR3BP alone, e.g., bifurcation analysis,[9] provides only limited clarity for the appearance of the three-lobe geometry in this region. This challenge of the CR3BP is often mitigated with extra computational efforts. The ER3BP, as an intermediate model, offers more informed predictions regarding the reference epoch, as the ER3BP structures are associated with particular values for the true anomaly that narrow the search space for the favorable reference epoch. Of course, it is emphasized that these benefits are valid for this sample orbit, and the results cannot be generalized to other regions across cislunar space. While the ER3BP does offer an improved estimate for the coefficients "on average", the structures from the ER3BP also may not maintain their geometries when parts of the trajectories are extremely sensitive to the difference in the coefficients. Also note that the ER3BP is not expected to deliver such an upgrade in the initial guess when the y-excursion of the s/c is non-negligible. In summary, while the ER3BP aids in the HFEM transition process for this sample orbit, the capabilities and limitations must be further verified in other regions in cislunar space.

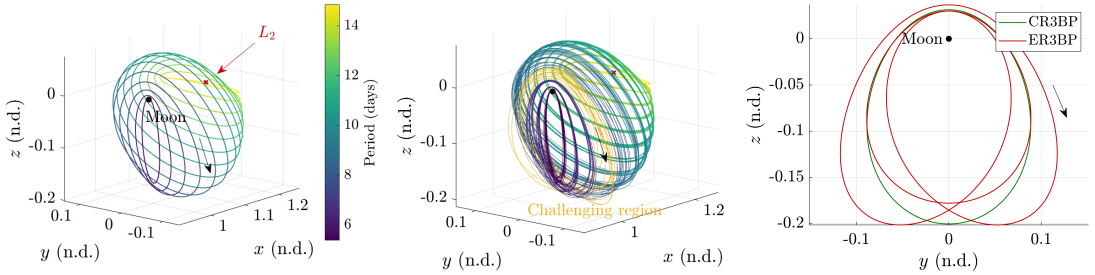

Figure 9: L_2 halo orbits in the CR3BP (left), transitioned results in the HFEM (center), and sample orbits within the challenging region

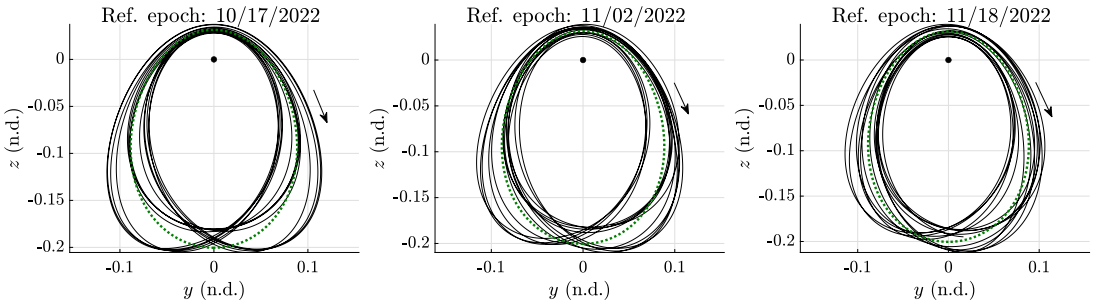

Figure 10: CR3BP results for selected epochs

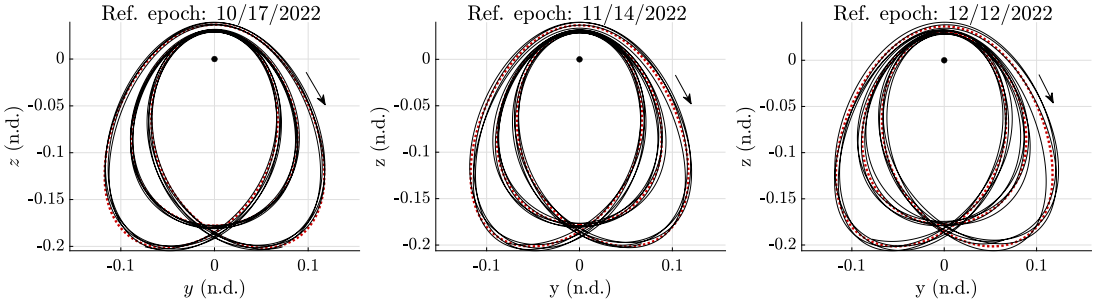

Figure 11: ER3BP results for selected epochs

In contrast, the BCR4BP is not expected to provide similar benefits in comparison with the ER3BP as an

intermediate model within the L_2 halo orbit family where the direct transition is challenging. However, within the same region, the BCR4BP does introduce a periodic orbit associated with a three-lobe geometry[18] that potentially serves as an enhanced initial guess, as investigated by Boudad, Howell and Davis.[9] While for some epochs, it is possible that the geometry of the transitioned solutions is consistent with that of the BCR4BP, recall that the additional acceleration in this region is dominated by the pulsation due to the relatively small y-excursions of the orbits. In Figure 12, the Earth-Moon distance is plotted on the left axis, and the Sun angle, θ_S, is plotted on the right axis over a time interval of 400 days. The cyan lines denote the epochs when $\theta_S = 0°$; in the BCR4BP, the three-lobe periodic orbit exists when the timing of the middle lobe apolune coincides with an epoch where $\theta_S = 0°$. Hence, it corresponds to a favorable reference epoch for the transition as observed in the BCR4BP. Three transition results are illustrated at three different reference epochs, utilizing the BCR4BP solution as the initial guess. For the case A, the transitioned solutions visually appears to maintain the three-lobe geometry as apparent in the BCR4BP. While this epoch indeed corresponds to an epoch when $\theta_S = 0°$, it is also noted that the Earth-Moon distance, l, is at a local minimum. Further examination reveals that this "perigee" epoch is indeed a reference epoch when the geometries are well maintained, not an epoch with $\theta_S = 0°$, illustrated by case B results. Thus, it is indicated that the geometries are more likely to be influenced by the pulsation, where the BCR4BP happens to provide similar geometry in position space.

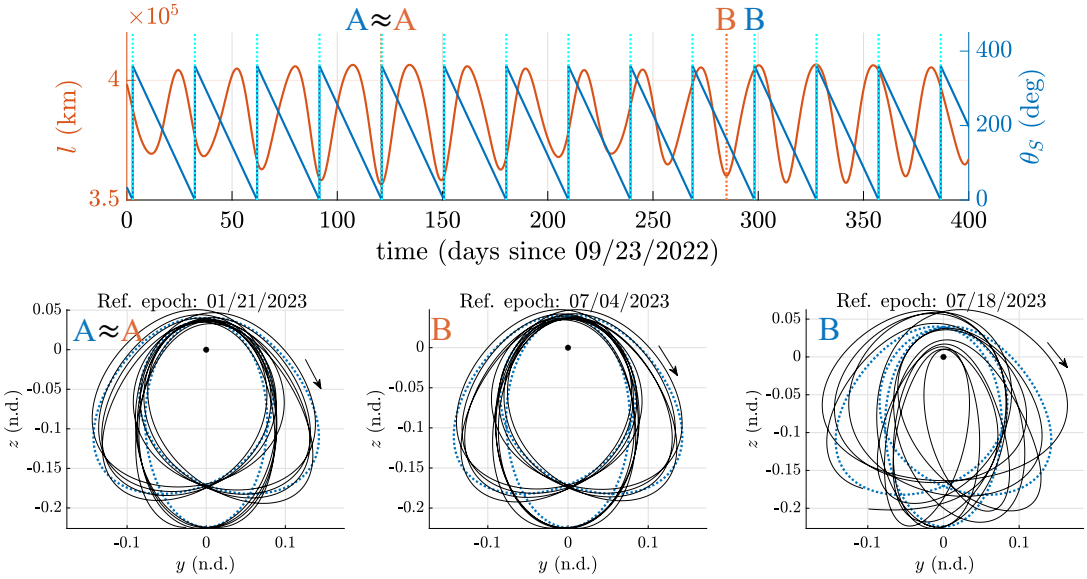

Figure 12: BCR4BP results for selected epochs

CONCLUDING REMARKS

The capabilities and limitations of the ER3BP and BCR4BP to serve as intermediate models are analyzed within the context of transition from the lower-fidelity CR3BP to an ephemeris model, HFEM, in cislunar space. The differential equations in the models are cast within a common, pulsating-rotating frame. The additional forces appearing in the HEFM are investigated and classified into two main sources: non-uniform pulsation of the Earth-Moon systen, and solar gravity. The rearranging of the solar gravity terms results in additional heuristics that the solar gravity contribution is mainly governed by terms that linearly depend on the y-excursion within the pulsating-rotating frame. The ER3BP and BCR4BP are then evaluated regarding their capabilities in describing the respective additional forces. While the capability of the ER3BP depends on the eccentricity value and the initial true anomaly, not surprisingly, it tends to better reflect the modeling of pulsation and line of apsides orientation on average as compared to the CR3BP, that is represented by the coefficients of the dynamical model. The BCR4BP is limited in estimating the actual solar perturbations that arise in the HFEM due to the fact that the Sun is not incorporated in a coherent manner. These findings are ap-

plied to a sample transition scenario for a member of the L_2 halo orbit family. For this sample transition case, the ER3BP provides benefits compared to the direct transition that solely depends on the CR3BP, whereas the BCR4BP is associated with some challenges as expected from the analysis of the dynamical models. The results here suggest a first step in a strategy to apply different intermediate models under various conditions.

APPENDIX A: DERIVATIONS OF EQUATION (22)

The acceleration terms in Eq. (21) are rearranged to yield cancellations and a more useful form. First, note that the relative acceleration of the Moon with respect to Earth is evaluated as follows,

$$\vec{A}_{EM} = -\frac{\tilde{\mu}_E+\tilde{\mu}_M}{R_{EM}^3}\vec{R}_{EM} + \sum_{j\in\mathcal{A}}\tilde{\mu}_j\left(\frac{1}{R_{jE}^3}\vec{R}_{jE} - \frac{1}{R_{jM}^3}\vec{R}_{jM}\right) = \frac{\tilde{\mu}_E+\tilde{\mu}_M}{l^2}\left(-\hat{x} + \sum_{j\in\mathcal{A}}\mu_j\left(\frac{1}{\rho_{jE}^3}\vec{\rho}_{jE} - \frac{1}{\rho_{jM}^3}\vec{\rho}_{jM}\right)\right). \tag{28}$$

Then, for the ephemeris model, $\ddot{\vec{\rho}}_{\mathcal{A}}$ is denoted as $\ddot{\vec{\rho}}_{\mathcal{A},H}$, where each coefficient in Eq. (21) is evaluated with instantaneous ephemerides data. The $\hat{x}$-component of $\ddot{\vec{\rho}}_{\mathcal{A},H}$ is evaluated as, $\ddot{\vec{\rho}}_{\mathcal{A},H}\cdot\hat{x} = b_1 + (b_7-1)x + b_9 y + b_8 z - \sum_{j\in\mathcal{A}}\frac{\mu_j}{\rho_{jc}^3}(x-x_j)$. Here, note that b_1 is evaluated as,

$$b_1 = \sum_{j\in\mathcal{A}}\mu_j\left(\frac{1-\mu}{\rho_{jE}^3}(-\mu-x_j) + \frac{\mu}{\rho_{jM}^3}(1-\mu-x_j)\right). \tag{29}$$

Next, b_7 results in the following,

$$\begin{aligned} b_7 - 1 &= -\frac{l''}{(t')^2 l} + \frac{h^2}{(t')^2 l^4} - 1 = -\frac{l(\vec{R}_{EM}\cdot\vec{A}_{EM} + V_{EM}^2) - l'(\vec{R}_{EM}\cdot\vec{V}_{EM})}{(t')^2 l^3} + \frac{l^2(V_{EM}^2 - l'^2)}{(t')^2 l^4} - 1 \\ &= -\frac{\vec{A}_{EM}\cdot\hat{x}}{(t')^2 l} - 1 = \sum_{j\in\mathcal{A}}\mu_j\left(\frac{1}{\rho_{jE}^3}(\mu+x_j) + \frac{1}{\rho_{jM}^3}(1-\mu-x_j)\right), \end{aligned} \tag{30}$$

where leveraging $\vec{R}_{EM} = l\hat{x}$, and $h = l\sqrt{V_{EM}^2 - l'^2}$. Similarly, b_8 is evaluated as,

$$b_8 = -\frac{1}{t'^2 l}\vec{A}_{EM}\cdot\hat{z} = \sum_{j\in\mathcal{A}}\mu_j\left(\frac{1}{\rho_{jE}^3}z_j - \frac{1}{\rho_{jM}^3}z_j\right). \tag{31}$$

Finally, b_9 results in,

$$b_9 = \frac{h'}{(t')^2 l^2} = \frac{\hat{z}\cdot(\vec{R}_{EM}\times\vec{A}_{EM})}{(t')^2 l^2} = \frac{1}{t'^2 l}\vec{A}_{EM}\cdot\hat{y} = \sum_{j\in\mathcal{A}}\mu_j\left(-\frac{1}{\rho_{jE}^3}y_j + \frac{1}{\rho_{jM}^3}y_j\right). \tag{32}$$

Repeating a similar process for $\ddot{\vec{\rho}}_{\mathcal{A},H}\cdot\hat{y}$ and $\ddot{\vec{\rho}}_{\mathcal{A},H}\cdot\hat{z}$ results in the following expression,

$$\begin{aligned} \ddot{\vec{\rho}}_{\mathcal{A},H} = &-\sum_{j\in\mathcal{A}}\mu_j\left(\frac{\vec{\rho}_{jc}}{\rho_{jc}^3} + \frac{\vec{\rho}_{Mc}\cdot\hat{x}}{\rho_{jE}^3}\vec{\rho}_{jE} - \frac{\vec{\rho}_{Ec}\cdot\hat{x}}{\rho_{jM}^3}\vec{\rho}_{jM} - \frac{\vec{\rho}_{Mc}\cdot\hat{y}}{\rho_{jE}^3}(\vec{\rho}_{jE}\times\hat{z}) + \frac{\vec{\rho}_{Ec}\cdot\hat{y}}{\rho_{jM}^3}(\vec{\rho}_{jM}\times\hat{z}) - (\frac{zz_j}{\rho_{jE}^3} - \frac{zz_j}{\rho_{jM}^3})\hat{x}\right)... \\ &+\begin{bmatrix}0 & 0 & 0\\ 0 & 0 & b_6\\ 0 & -b_6 & 0\end{bmatrix}\dot{\vec{\rho}} + \begin{bmatrix}0 & 0 & 0\\ 0 & b_{12}-b_{12a} & b_{11}\\ 0 & -b_{11} & b_{12}-b_{12a}\end{bmatrix}\vec{\rho}. \end{aligned} \tag{33}$$

The above equation is the same as Eq. (22), concluding the derivations.

APPENDIX B: DERIVATIONS OF EQUATION (24)

Further simplification of Eq. (22) for $\ddot{\vec{\rho}}_{\mathcal{A},H}$ is deduced from the additional assumptions. Assuming that $\rho_j >> 1$, the inverse cubes of distance from j to the s/c, Earth, Moon, are linearized as,

$$\frac{1}{\rho_{jc}^3} \approx \frac{1}{\rho_j^3} + \frac{3}{\rho_j^5}(x_j x + y_j y + z_j z), \quad \frac{1}{\rho_{jE}^3} \approx \frac{1}{\rho_j^3} + \frac{3}{\rho_j^5}x_j(-\mu), \quad \frac{1}{\rho_{jM}^3} \approx \frac{1}{\rho_j^3} + \frac{3}{\rho_j^5}x_j(1-\mu), \tag{34}$$

respectively. Utilizing these linearized functions, the expressions for the terms in Eq. (22) are reduced to simpler formulations. For the $\hat{x}$-direction, the resulting expression is,

$$\ddot{\vec{\rho}}_{\mathcal{A},H} \cdot \hat{x} \approx \sum_{j \in \mathcal{A}} (\frac{3\mu_j}{\rho_j^5} \cdot 2x_j y_j y). \tag{35}$$

Next, the approximate accelerations for the $\hat{y}$ and $\hat{z}$-directions are evaluated as,

$$\ddot{\vec{\rho}}_{\mathcal{A},H} \cdot \hat{y} \approx \sum_{j \in \mathcal{A}} \frac{3\mu_j}{\rho_j^5} \left((y_j^2 - x_j^2)y + y_j z_j z\right) + (b_{12} - b_{12a})y + b_{11}z + b_6 \dot{z} \tag{36}$$

$$\ddot{\vec{\rho}}_{\mathcal{A},H} \cdot \hat{z} \approx \sum_{j \in \mathcal{A}} \frac{3\mu_j}{\rho_j^5} \left(y_j z_j y + z_j z_j z\right) - b_{11}y + (b_{12} - b_{12a})z - b_6 \dot{y}, \tag{37}$$

where coefficients are also well approximated as,

$$b_6 \approx K_1 \sum_{j \in \mathcal{A}} \frac{3\mu_j}{\rho_j^5} x_j z_j, \quad b_{11} \approx K_2 \sum_{j \in \mathcal{A}} \frac{3\mu_j}{\rho_j^5} x_j z_j + K_3 \sum_{j \in \mathcal{A}} \frac{3\mu_j}{\rho_j^5} x_j \dot{z}_j, \quad b_{12} - b_{12a} \approx K_4 (\sum_{j \in \mathcal{A}} \frac{3\mu_j}{\rho_j^5} x_j z_j)^2, \tag{38}$$

where K_{1-4} are functions of ephemerides, e.g., $K_1 = 2l^2 t'/h$. Additionally, if additional bodies are negligible except for the Sun, and assuming that $|z_S| << \rho_S$, or the $\hat{z}$-component of the solar position is negligible, the following linearized expression is produced,

$$\ddot{\vec{\rho}}_{\mathcal{A},H} \approx \ddot{\vec{\rho}}_{\mathcal{A},L} := \frac{3\mu_S}{\rho_S^5} \left(2x_S y_S y\hat{x} + (y_S^2 - x_S^2)y\hat{y}\right) = \frac{3\mu_S}{\rho_S^3} y(\sin 2\theta_S \hat{x} - \cos 2\theta_S \hat{y}), \tag{39}$$

concluding the derivations of Eq. (24).

ACKNOWLEDGEMENTS

The authors would like to thank Kenza Boudad and rest of the Multi-Body Dynamics Group members for insightful discussions. The first author would like to thank Kwanjeong Educational Foundation for the financial support. Support from NASA Johnson Space Center under cooperative agreement Number 80NSSC18M0122 is appreciated.

REFERENCES

[1] V. Angelopoulos, "The ARTEMIS Mission," *Space Science Reviews*, Vol. 165, No. 1, 2011, pp. 3–25, 10.1007/s11214-010-9687-2.

[2] K. Oguri, K. Oshima, S. Campagnola, K. Kakihara, N. Ozaki, N. Baresi, Y. Kawakatsu, and R. Funase, "EQUULEUS Trajectory design," *The Journal of the Astronautical Sciences*, Vol. 67, No. 3, 2020, pp. 950–976.

[3] J. C. Crusan, R. M. Smith, D. A. Craig, J. M. Caram, J. Guidi, M. Gates, J. M. Krezel, and N. B. Herrmann, "Deep Space Gateway Concept: Extending Human Presence into Cislunar Space," *2018 IEEE Aerospace Conference*, IEEE, 2018, pp. 1–10.

[4] D. A. Dei Tos and F. Topputo, "Trajectory refinement of three-body orbits in the real solar system model," *Advances in Space Research*, Vol. 59, Apr. 2017, pp. 2117–2132, 10.1016/j.asr.2017.01.039.

[5] Z. P. Olikara, *Computation of quasi-periodic tori and heteroclinic connections in astrodynamics using collocation techniques*. PhD Dissertation, University of Colorado at Boulder, 2016.

[6] C. Ocampo, "An Architecture for a Generalized Spacecraft Trajectory Design and Optimization System," *Libration Point Orbits and Applications*, 2003, pp. 529–571, 10.1142/9789812704849_0023.

[7] D. C. Davis, S. M. Phillips, K. C. Howell, S. Vutukuri, and B. P. McCarthy, "Stationkeeping and transfer trajectory design for spacecraft in cislunar space," *AAS/AIAA Astrodynamics Specialist Conference*, 2017, pp. 1–20.

[8] J. Williams, D. Lee, R. Whitley, K. Bokelmann, D. Davis, and C. Berry, "Targeting Cislunar Near Rectilinear Halo Orbits for Human Space Exploration," *27th AAS/AIAA Space Flight Mechanics Meeting*, 2017.

[9] K. Boudad, K. C. Howell, and D. C. Davis, "Analogs for Earth-Moon Halo Orbits and their Evolving Characteristics in Higher-Fidelity Force Models," *AIAA SCITECH 2022 Forum*, 2022, p. 1276.

[10] G. Lantoine and R. P. Russell, "Near ballistic halo-to-halo transfers between planetary moons," *The Journal of the Astronautical Sciences*, Vol. 58, No. 3, 2011, pp. 335–363.

[11] H. Peng and X. Bai, "Natural deep space satellite constellation in the Earth-Moon elliptic system," *Acta astronautica*, Vol. 153, 2018, pp. 240–258.

[12] D. A. Dei Tos and F. Topputo, "On the advantages of exploiting the hierarchical structure of astrodynamical models," *Acta Astronautica*, Vol. 136, July 2017, pp. 236–247, 10.1016/j.actaastro.2017.02.025.

[13] M. Jorba-Cuscó, A. Farrés, and À. Jorba, "Two periodic models for the Earth-Moon system," *Frontiers in Applied Mathematics and Statistics*, Vol. 4, 32, 2018, pp. 1–14.

[14] G. Gómez, J. J. Masdemont, and J. M. Mondelo, "Solar system models with a selected set of frequencies," *Astronomy & Astrophysics*, Vol. 390, Aug. 2002, pp. 733–749, 10.1051/0004-6361:20020625.

[15] X. Hou and L. Liu, "On quasi-periodic motions around the triangular libration points of the real Earth–Moon system," *Celestial Mechanics and Dynamical Astronomy*, Vol. 108, No. 3, 2010, pp. 301–313.

[16] X. Hou and L. Liu, "On quasi-periodic motions around the collinear libration points in the real Earth–Moon system," *Celestial Mechanics and Dynamical Astronomy*, Vol. 110, No. 1, 2011, pp. 71–98.

[17] A. Jorba and J. Villanueva, "On the persistence of lower dimensional invariant tori under quasi-periodic perturbations," *Journal of Nonlinear Science*, Vol. 7, No. 5, 1997, pp. 427–473.

[18] K. K. Boudad, K. C. Howell, and D. C. Davis, "Dynamics of synodic resonant near rectilinear halo orbits in the bicircular four-body problem," *Advances in Space Research*, Vol. 66, No. 9, 2020, pp. 2194–2214.

[19] F. Ferrari and M. Lavagna, "Periodic motion around libration points in the elliptic restricted three-body problem," *Nonlinear Dynamics*, Vol. 93, No. 2, 2018, pp. 453–462.

[20] C. Acton, N. Bachman, B. Semenov, and E. Wright, "A Look Toward the Future in the Handling of Space Science Mission Geometry," *Planetary and Space Science*, Vol. 150, 2018, pp. 9–12.

[21] D. A. Dei Tos, "Automated Trajectory Refinement of Three-Body Orbits in the Real Solar System Model," M.S. Thesis, Politecnico di Milano, Italy, 2014.

[22] V. Szebehely, *Theory of orbit: The restricted problem of three Bodies*. Academic Press, 1967.

[23] S. Scheuerle, "Construction of ballistic lunar transfers in the earth-moon-sun system," M.S. Thesis, Purdue University, West Lafayette, Indiana, 2021.

[24] G. Gómez, A. Jorba, C. Simó, and J. Masdemont, *Dynamics and Mission Design Near Libration Points: Volume III: Advanced Methods for Collinear Points*. World Scientific, 2001.

[25] B. Park, "Low-Thrust Trajectory Design for Tours of the Martian Moons," M.S. Thesis, Purdue University, West Lafayette, Indiana, 2021.

[26] A. Hoffman, B. Park, T. Roorda, S. Stewart, and K. Howell, "Trajectory Design for a Secondary Payload within a Complex Gravitational Environment: The Khon-1 Spacecraft," *2022 AAS/AIAA Astrodynamics Specialist Conference*, 2021.

[27] X. Y. Hou and L. Liu, "On quasi-periodic motions around the triangular libration points of the real Earth–Moon system," *Celestial Mechanics and Dynamical Astronomy*, Vol. 108, Nov. 2010, pp. 301–313, 10.1007/s10569-010-9305-3.